# Performance of Beam-Column Connections with Mass Ply Lam and Steel Dowels under Cyclic Loads

Emily Williamson, S.M.ASCE[1]; Chris P. Pantelides, F.ASCE[2]; Hans-Erik Blomgren, M.ASCE[3]; and Douglas Rammer, M.ASCE[4]

**Abstract:** A mass timber lateral force resisting system (LFRS) is proposed using a mass timber buckling restrained brace (TBRB) to improve the seismic resilience of mass timber buildings. To develop a resilient braced frame, it is essential to understand and quantify the behavior of the connections, including the possible failure modes and moment-rotation capacities. Cyclic and monotonic tests were conducted on six mass timber beam-column connections to study the response of a mass timber joint connected with slotted-in steel plates and mild steel dowels. The primary goal of the subassembly tests was to measure the maximum rotation, stiffness, ductility, and failure modes of such connections for both monotonic and cyclic loads. The tests showed that the connections with three steel dowel details reached a maximum rotation of 0.11 radians (6.3 degrees) with no loss of strength. In addition, a numerical model was developed to represent the moment-rotation relationship of the mass timber beam-column connections. **DOI: 10.1061/JSENDH.STENG-11569.** 

**Author keywords:** Beam-column connection; Cyclic test; Experiment; Mass ply lam; Monotonic test; Numerical model; Steel dowel.

## Introduction

Mass timber has recently become a popular option as a primary structural material for new buildings in the United States. Mass timber has many benefits; it is light-weight, sustainable, fast to construct due to prefabrication, and has architectural appeal. There are many engineered timber products used in practice: glued laminated timber, laminated veneer lumber (LVL), cross laminated timber (CLT), dowel laminated timber (DLT), nail laminated timber (NLT), laminated strand lumber (LSL), and particle strand lumber (PSL), to name a few. These materials have allowed engineers to take advantage of mass timber's benefits because the materials are made up of sorted layers of the strongest, most ideal parts of a tree. Mass ply panel (MPP) and mass ply lam (MPL) have recently entered the market as new classes of CLT and LVL, respectively (APA 2021); these materials use veneers with different cross-grain directions to make 25.4 mm (1-in.) layers, which are pressed together with adhesive to produce the desired section thickness. The layup of the MPL presents certain advantages compared with other engineered timber materials. The cross-ply veneers within the layup provide increased stiffness in the perpendicular-to-grain direction; therefore, MPL is essentially self-reinforced by these veneers. Additionally, MPL is very dimensionally stable for moisture; this allows designers to avoid additional requirements defined in the National Design Specification for Wood Construction (NDS) for fastener spacing in deep beams. The alternate cross grains provide strength and dimensional stability in the perpendicular-to-grain direction to arrest member splitting potential, which is a limiting factor in connection design.

Current tall mass timber buildings consist of a timber gravity system combined with a steel or concrete lateral force resisting system (LFRS). The combination of materials can lead to compatibility issues due to the ways differing materials deform when loaded under time varying dynamic loads, such as those occurring in earthquakes. In addition to avoiding compatibility issues, using mass timber for the entire structural system allows the designer to take full advantage of timber's many benefits. A uniform structural building material also benefits the construction of the building because it reduces risk on the construction site, limits the need for coordination between multiple trades onsite, and reduces the time for construction. To expand the applications of mass timber in new building construction, a wider variety of timber LFRSs must be developed and adopted by building codes. Existing wood LFRSs include conventional timber braced frames and wood framed shear walls. Timber braced frames lack code definition; ASCE-7 (ASCE 2016) does not have defined $R$, $C_d$, or $\boldsymbol{\Omega}_o$ values, nor is there a defined design method in the NDS. Conventional timber braced frames do not provide adequate ductility to be used for tall buildings in high seismic regions because they rely on the end connections of the brace, which provide relatively small hysteretic energy dissipation and limited drift capacity. Cao et al. (2022) completed full-scale experimental testing and parametric studies with a simplified model to evaluate the seismic performance of a timber frame with bolted connections similar to the connections used in conventional timber braced frames. The use of wood shear walls poses its own challenges as an LFRS solution, because walls do not always allow for the floor plan flexibility that is often preferred by building users. Slip friction joints (RSFJ) have also been studied as a solution for decreasing residual drift and floor acceleration in timber buildings (Hashemi et al. 2016, 2018, 2020). Similarly, perforated steel plates have been used as energy dissipators in CLT shear walls as panel connectors or hold-downs (Daneshvar et al. 2022).

[1]Graduate Research Assistant, Dept. of Civil and Environmental Engineering, Univ. of Utah, Salt Lake City, UT 84112. ORCID: https://orcid.org/0000-0003-0927-0771. Email: emily.diedrich@utah.edu

[2]Professor, Dept. of Civil and Environmental Engineering, Univ. of Utah, Salt Lake City, UT 84112 (corresponding author). ORCID: https://orcid.org/0000-0003-3309-3488. Email: c.pantelides@utah.edu

[3]Structural Engineer, Timberlab, 1601 NE Columbia Blvd., Portland, OR 97211. Email: hans-erik.blomgren@timberlab.com

[4]Research Engineer, Forest Products Laboratory, One Gifford Pinchot Dr. Madison, WI 53726. Email: douglas.r.rammer@usda.gov

Note. This manuscript was submitted on April 12, 2022; approved on December 16, 2022; published online on March 28, 2023. Discussion period open until August 28, 2023; separate discussions must be submitted for individual papers. This paper is part of the ***Journal of Structural Engineering***, © ASCE, ISSN 0733-9445.

Buckling-restrained-brace frames (BRBF) are commonly used as the LFRS in steel buildings located in high seismic zones (i.e., seismic design categories D, E and F). A BRBF includes a frame with steel beams and columns and a diagonal buckling-restrained-brace (BRB). The conventional BRB is constructed of an unbonded steel yielding core encased in a concrete-filled steel tube. The design of this type of brace allows it to have balanced capacities in tension and compression because the yielding core elongates in tension but is restrained from buckling in compression by the casing. Steel-concrete BRBs have been tested extensively and have been proven to dissipate energy efficiently and perform well during strong earthquakes. Previous BRB tests resulted in stable hysteresis curves with practically no pinching, thus allowing higher energy dissipation compared with other types of steel braces (Black et al. 2004; Fahnestock et al. 2007; Wu et al. 2014; Xu and Pantelides 2017). Buckling-restrained braced frames have also been found to be effective in reducing residual drift when combined with special moment resisting frames in a dual system (Sabelli et al. 2003; Kiggins and Uang 2006).

Based on principles similar to the design of a conventional BRB, a timber BRB (TBRB) was developed and tested using both fatigue and high-strain cyclic loading protocols (Murphy et al. 2021). Similar to a conventional BRB, the TBRB uses a steel yielding core to achieve high ductility and balanced strengths in tension and compression. However, instead of a concrete casing, the TBRB's yielding steel plate core is sandwiched between MPP blocks that are bolted together. During the experiments, the TBRB achieved cumulative inelastic deformations ranging from 2.4 to 7.8 times the AISC 341 minimum requirement for conventional BRBs (AISC 2016). Moreover, the TBRB achieved up to 3.9% strain compared with the typical 3.0% to 3.5% maximum strain observed in conventional BRBs (Xu and Pantelides 2017). Before a TBRB can be used as part of an LFRS, more testing must be completed to observe the performance of the entire TBRB frame (TBRBF) system. Dong et al. (2020) successfully tested a mass timber frame with two conventional BRBs in a chevron configuration using two connection types: dowelled connections with slotted-in steel plates, and screwed connections with steel side plates. During testing, the frame was able to reach 1.5% story drift before the capacity of the actuator was reached, and the beam-column connections experienced minimal damage. The results of that study demonstrate the potential for mass timber BRBFs. Moreover, full building computational studies have also been completed to demonstrate the feasibility of a TBRBF (Blomgren et al. 2016).

In order to take full advantage of a TBRB, it is important to design beam-column connections that can withstand demands from lateral loads such that the TBRB core plate is the primary yielding mechanism in accordance with capacity-based design principles. To properly design a TBRBF, the connection performance must be understood, which includes the potential failure modes and the moment-rotation capacity of the connections. It is important to know if additional reinforcement will be required to improve the performance of the timber connections and restrain perpendicular-to-grain splitting. It is beneficial to design a connection that does not require additional joint reinforcement, because the cost and additional labor associated with timber connections is a primary deterrent when considering mass timber as a structural solution (Blaß and Schädle 2011).

Researchers have been interested in the performance of heavy timber connections for some time (Rebouças et al. 2022). Several studies have been completed focusing on the design and performance of timber connections with glued-in rods (Ogrizovic et al. 2017; Steiger et al. 2015; Fragiacomo and Batchelar 2012). Lam et al. (2008) studied the performance of bolted timber moment resisting connections. Other studies have examined the influence of steel properties on the ductility of doweled timber connections (Geiser et al. 2021). Tests were completed on single-dowel steel-to-timber connections to evaluate the load-carrying behavior of these types of connections (Dorn et al. 2013). The performance of different connectors (such as bolts and rivets) under monotonic and cyclic loading protocols have been compared (Popovski et al. 2002). The impact of edge distance, number of fasteners, and the use of self-tapping screws as additional joint reinforcement on the moment capacity of bolted glulam beam-column connections has been studied (Petrycki and Salem 2020). Furthermore, the use of glued-in steel plates for mass timber composite connections has been explored, although these connections are often limited by epoxy failure (Otero-Chans et al. 2018).

Previous studies observed the moment-rotation capacity of timber connections using glulam beam and column members. Dong et al. (2021) tested connections with glulam members, steel plates, and self-drilling dowels. Part of the study included observing the difference in performance under cyclic loading between connections with and without joint reinforcing. The unreinforced connection achieved an average ultimate rotation of 0.02 radians (1.1 degrees) before failure and the reinforced connection achieved an average ultimate rotation of 0.06 radians (3.4 degrees) before failure. Bouchaïr et al. (2007) studied the interaction of dowels in a circular layout in a moment connection; these joints also required reinforcement to achieve higher rotations.

This paper discusses the design, testing, and performance of six MPL beam-column connections. The design of the connection aimed to achieve a ductile response and to avoid the requirement for supplemental joint reinforcement to prevent brittle timber splitting failure modes. In addition, a numerical model of the connection behavior was developed in OpenSees (McKenna et al. 2010). The experimental results combined with the numerical model provide an improved understanding of the connection moment-rotation behavior, which can be considered during the design of future timber frames. The model for predicting the moment capacity of the connection developed by Bouchaïr et al. (2007) is adopted in this study to predict the capacity of the connections tested.

## Connection Design

The connection tested in this experimental program is based on the expected design for a beam-column-brace joint in a TBRBF specimen, shown in Fig. 1. The frame has a beam span of 4.27 m (14 ft) and a story height of 2.90 m (9 ft–6 in.). The lengths for the members represent the distances to the theoretical inflection points at mid-beam span and mid-column height. The beam-column connection uses dowels and two steel plates inserted into slots cut in the beam and column.

For testing convenience, the joint was rotated 1.57 radians (90 degrees) counterclockwise; thus the beam was the vertical component during testing, as shown in Fig. 2. For the beams and columns, 389 mm (15–5/16 in.) by 381 mm (15 in.) F16 MPL (APA 2021) sections were used with a modulus of elasticity of 11 GPa (1,600 ksi). The elastic modulus for MPL was achieved using seven long-plies per 25 mm (1 in.) and two cross-plies per 25 mm (1 in.) (Murphy et al. 2021). The beam and column members were connected with two 13 mm (1/2 in.) thick slotted-in steel plates with a nominal yield stress of 248 MPa (36 ksi). A number of smooth-shank mild steel dowels with a 13 mm (1/2-in.) diameter and a nominal yield stress of 248 MPa (36 ksi) were used to connect the entire assembly. Computer numerical control (CNC) machines were used to cut the holes for the dowels in the steel plates and the





J. Struct. Eng., 2023, 149(6): 04023057

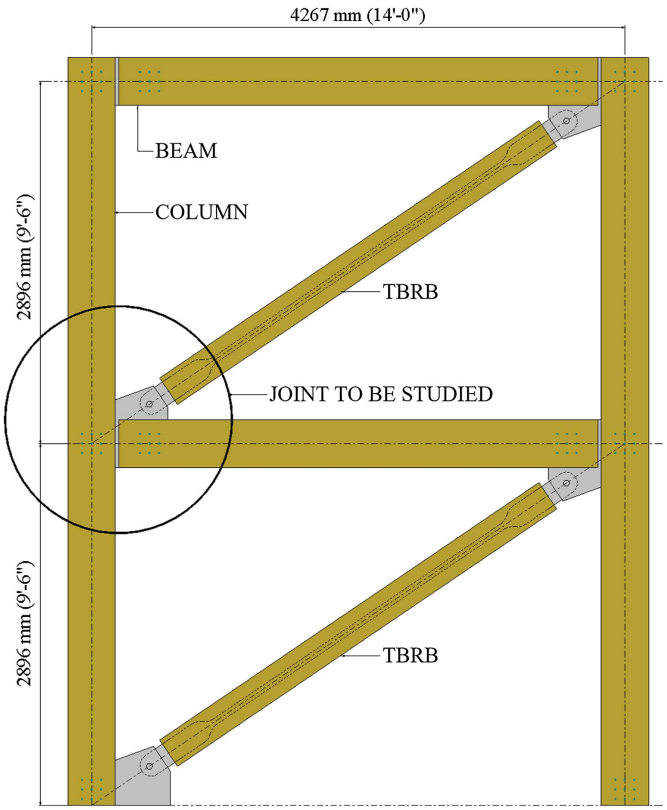


**Fig. 1.** TBRBF for basis of design.

MPL members to help ensure the dowel hole alignment. The dowel number and layout were chosen to meet the demand from the TBRB in the TBRBF shown Fig. 1. The capacity of the connection was evaluated according to the NDS (AWC 2018b). The NDS Technical Report 12 (AWC 2018a) includes design equations that consider four possible failure modes for single-dowel connections in single and double shear. Each applicable yield mode must be evaluated and the mode with the minimum yield force controls the design. Yield mode I is governed by uniform dowel bearing in the main member or the side members. The yield value is determined by:

$$P_m = 2q_m L_m \tag{1}$$

$$P_s = 2q_s L_s \tag{2}$$

where $P_m$ and $P_s$ are the yield values for the main and side members, respectively; $q_m$ and $q_s$ are the main member or side member dowel bearing strengths times the dowel diameter; and $L_m$ and $L_s$ are the lengths of the main member or side member, respectively.

Yield mode II is limited by dowel bearing in both the side and main members, but applies only to single shear connections. Yield modes III and IV are calculated based on:

$$P = \frac{-B + \sqrt{B^2 - 4AC}}{2A} \tag{3}$$

Mode $\mathrm{III_m}$ is governed by dowel bearing within the main member and dowel bending in the side member, although it only applies to single shear connections. Mode $\mathrm{III_s}$ is limited by dowel bearing in the side member and dowel bending in the main member. It is evaluated using the following equations:

$$A = \frac{1}{4q_s} + \frac{1}{2q_m} \tag{4}$$

$$B = \frac{L_s}{2} + g \tag{5}$$

$$C = \frac{-q_s L_s^2}{4} - M_m \tag{6}$$

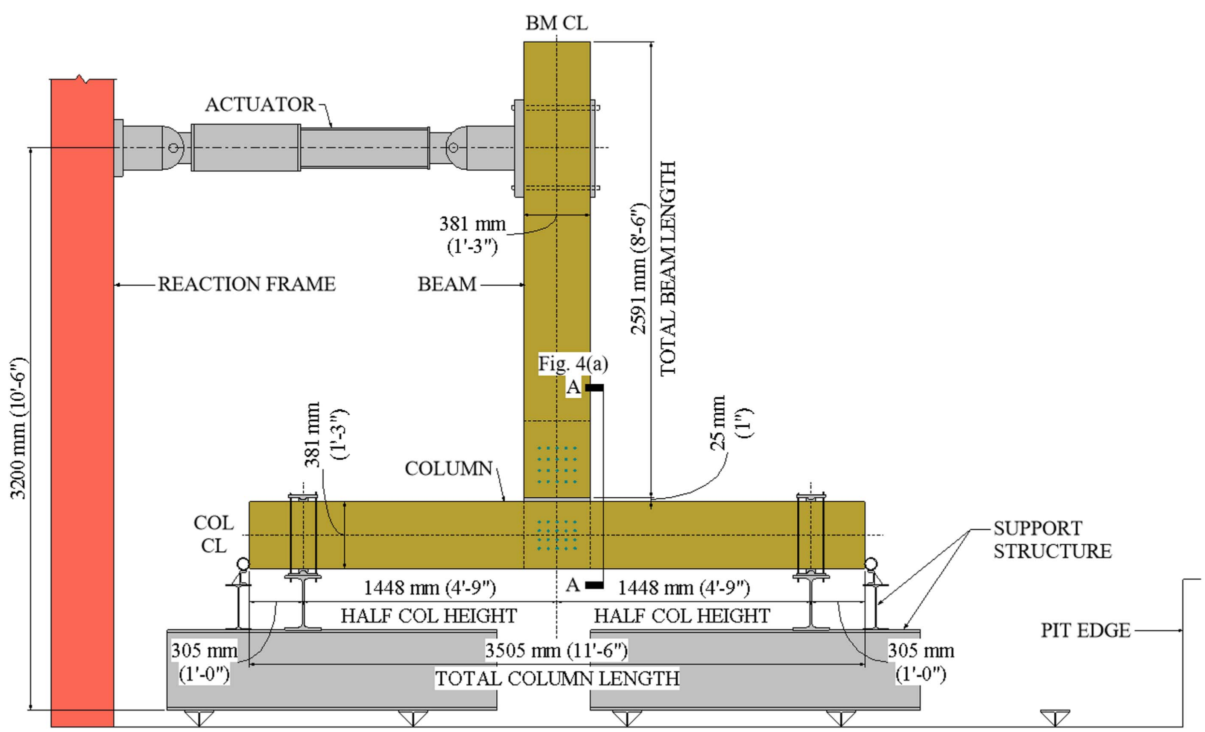


**Fig. 2.** Schematic of joint test configuration.



J. Struct. Eng., 2023, 149(6): 04023057

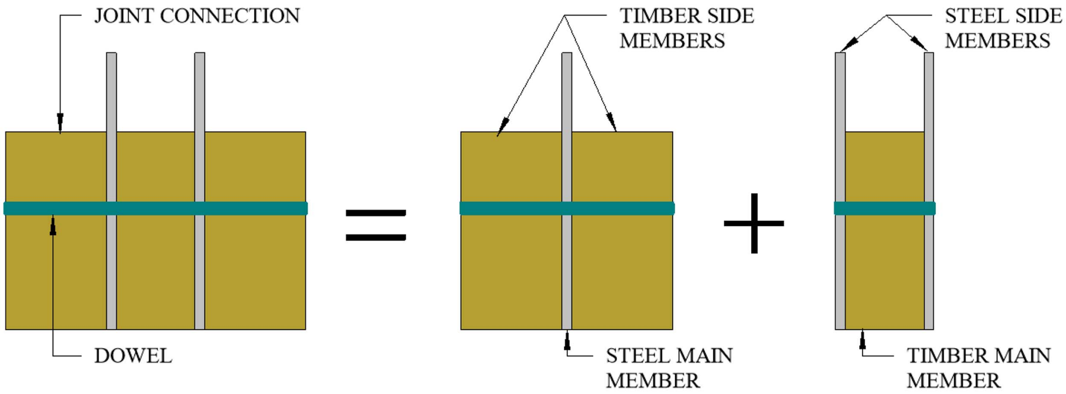


**Fig. 3.** Connection equivalent model. (Adapted from Fan et al. 2011.)

where $g$ is the gap between the main member and side member; and $M_m$ is the maximum moment developed in the main member. Finally, mode IV is limited by dowel bending in the main and side members and is evaluated using:

$$A = \frac{1}{2q_s} + \frac{1}{2q_m} \tag{7}$$

$$B = g \tag{8}$$

$$C = -M_s - M_m \tag{9}$$

where $M_s$ is the maximum moment developed in the side member. The dowel diameter and plate thickness were chosen such that the governing yield mode of the connection was mode IV, because the yielding of dowels allows for a ductile response. The design force, $Z$, for the single-dowel connection is determined by dividing the minimum yield force, $P$, by a reduction factor, $R_d$, which depends on the angle of the force in the dowel to the grain of the timber and the yield mode being evaluated. In this study, forces were considered to be applied to the connection both perpendicular and parallel to the grain due to the horizontal and vertical components of the TBRB axial force; therefore, $R_d$ factors of 4.0 and 3.2 were used for the perpendicular and parallel-to-grain directions, respectively. Next, the design force is multiplied by a load duration factor, $C_D$. This design used a load duration factor equal to 1.6 because the connection is designed for a seismic application. In addition to designing the connection based on allowable stress design (ASD), the design was checked against the capacity determined with the NDS load and resistance factor design (LRFD) values to be consistent with the capacity-based principles used for BRB design.

The connections used in this study have five components: three mass timber sections and two steel plates. Therefore, the NDS equations do not directly relate to the design of the connection because they are based on three-member connections. In order to calculate the capacity of the connection using the NDS equations, the connection is represented by an equivalent model developed by Fan et al. (2011). The equivalent model evaluates the connection as two separate three-member connections in series, as shown in Fig. 3. The first part in the series is a three-member connection with the steel plate as the main member and timber sections as the side members; the second part is a three-member connection with the timber section as the main member and the steel plates as the side members. The NDS equations described prevviously were evaluated for each element of the equivalent model. The individual design values were combined using Eq. (10) to obtain the design capacity of a single-dowel beam-column connection, using Fig. 3 and following the procedure by Fan et al. (2011):

$$Z = Z_{\text{steel main member}} + (n_s - 1)Z_{\text{timber main member}} \tag{10}$$

where $n_s$ is the number of steel plates in the connection; and $Z_{\text{steel main member}}$ and $Z_{\text{timber main member}}$ are the controlling design forces for double shear connections, determined based on the controlling yield mode for the connection where steel and timber act as the main member, respectively.

The NDS equations (AWC 2018b) and equivalent model described previously provide the capacity of a connection with a single dowel. The load capacity of a connection with multiple dowels is not directly proportional to the number of dowels in a row because the load does not distribute evenly among the dowels; therefore, the NDS requires the application of a group reduction factor when designing a connection with multiple connectors:

$$C_g = \frac{m(1-m^{2n})}{n[(1+R_{\text{EA}}m^n)(1+m) - 1 + m^n} \quad \frac{1+R_{\text{EA}}}{1-m} \tag{11}$$

$$R_{\text{EA}} = \text{min of } \frac{E_s A_s}{E_m A_m}, \frac{E_m A_m}{E_s A_s} \tag{12}$$

$$m = u - \sqrt{u^2 - 1} \tag{13}$$

$$u = 1 + \gamma \frac{s}{2} \; \frac{1}{E_m A_m} + \frac{1}{E_s A_s} \tag{14}$$

where $n$ is the number of fasteners in a row; $E_m$, $E_s$ is the modulus of elasticity of the main and side members; $A_m$, $A_s$ is the gross cross-sectional area of the main and side members; $s$ is the center-to-center spacing between fasteners, and the load slip modulus $\gamma$ is defined as:

$$\gamma = 369.37D^{1.5} \text{ (SI Units)} \tag{15a}$$

$$\gamma = 270{,}000 \; D^{1.5} \text{(US Units)} \tag{15b}$$

where $D$ is the dowel diameter (FPL 2010). For this connection design, 0.93 was applied as the group factor.

The connections designed and tested during this study are intended to be part of an TBRBF, as shown in Fig. 1, so they were designed to resist the overstrength forces of a TBRB in tension and compression. The overstrength factors were selected based on the results presented in Murphy et al. (2021); in the present study a compression adjustment factor equal to 1.25 and a strain hardening



J. Struct. Eng., 2023, 149(6): 04023057

adjustment factor equal to 1.45 were used. The expected axial force in the TBRB is 494 kN (111 kips) in compression and 396 kN (89 kips) in tension. Thus, the design of the connection is controlled by the brace compression forces, and the connection must withstand tension forces with a horizontal component of 409 kN (92 kips) and a vertical component of 280 kN (63 kips). Using the procedure discussed previously, it was determined that the connection required twenty dowels in the beam and twenty dowels in the column. The dowels were spaced four times the diameter of the dowel apart, per the minimum requirement set by the NDS. Due to the large axial force expected in the beam, the dowel spacing along the L-axis (ASTM 2019) of the timber was increased from 51 to 64 mm (2.0 to 2.5 in.) along the axis parallel to the grain of the timber to avoid failure caused by local stresses in the timber within the dowel group, as recommended in NDS Appendix E (AWC 2018b). In a TBRBF, the gusset plates for the TBRB will be extensions of the connection plates. For testing simplicity, these extensions were not included in these tests. However, the influence of the brace is likely to impact the performance of the connection, thus further testing of the system with a TBRB is necessary. The final design and

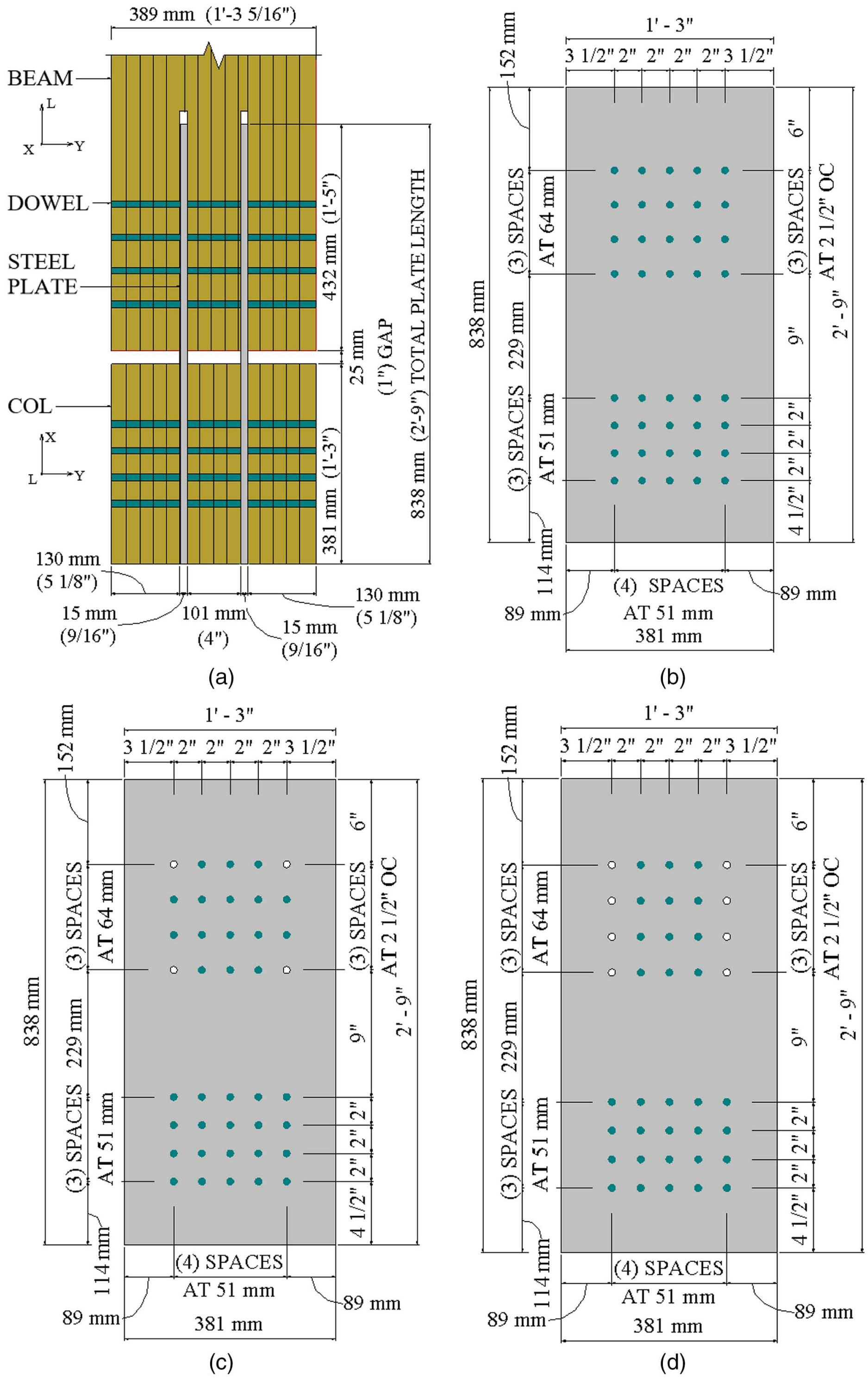


**Fig. 4.** Joint details: (a) section A-A; (b) joints J20M and J20C; (c) joints J16M and J16C; and (d) joints J12M and J12C.

**Table 1.** Joint test matrix

| Joint | Test type | Number of dowels in beam | Number of dowels in column |
|---|---|---|---|
| 20M | Monotonic | 20 | 20 |
| 16M | Monotonic | 16 | 20 |
| 12M | Monotonic | 12 | 20 |
| 20C | Cyclic | 20 | 20 |
| 16C | Cyclic | 16 | 20 |
| 12C | Cyclic | 12 | 20 |

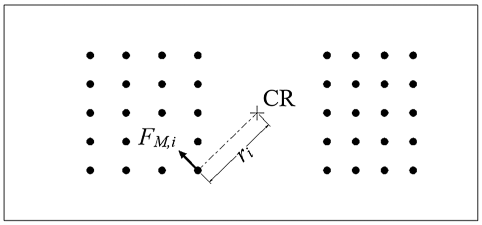


**Fig. 5.** Moment capacity model.

**Table 2.** Joint capacities

| Joint | Theoretical moment capacity kN-m (kip-in.) |
|---|---|
| 20M, 20C | 104 (921) |
| 16M, 16C | 91 (809) |
| 12M, 12C | 79 (699) |

dowel layout of the connection is shown in Figs. 4(a and b). In order to observe the impact of different dowel layouts on the moment-rotation relationship, two additional layouts were tested: one with sixteen dowels and one with twelve dowels in the beam [Figs. 4(c and d)]. All joints had twenty dowels in the column. Table 1 lists the test types and dowel layouts for each joint test.

After designing the connection, a theoretical bending moment capacity for each connection was determined using the equation described by Bouchaïr et al. (2007), which relates the force resisted by each dowel to the distance the dowel is from the center of rotation of the connection, given as:

$$M = \sum_{i=1}^{n} F_{M,i} r_i \tag{16}$$

where $M$ is the bending moment capacity of the connection; $F_{M,i}$ is the force in fastener $i$; and $r_i$ is the distance from the rotational center of fastener $i$, as shown in Fig. 5. Because the group factor, $C_g$, was applied in the design of the connections, as indicated in Eq. (11), this model assumes that the axial forces in the beam and column members are equally distributed as shear forces in the dowels; the moment component of the load is distributed proportionally to the distance from the center of rotation. The rotational center is located at the geometric center of the dowel layout. The theoretical moment capacity based on the ASD strength obtained for the three joint configurations is shown in Table 2.

Finally, a 25 mm (1-in.) gap was left between the beam and the column to allow rotation of the beam to occur without making contact with the column [Fig. 4(a)]. This was done in an attempt to increase the amount of rotation achieved by the connection by eliminating the additional stress in the members due to contact between them. In previous experimental programs (Dong et al. 2021;

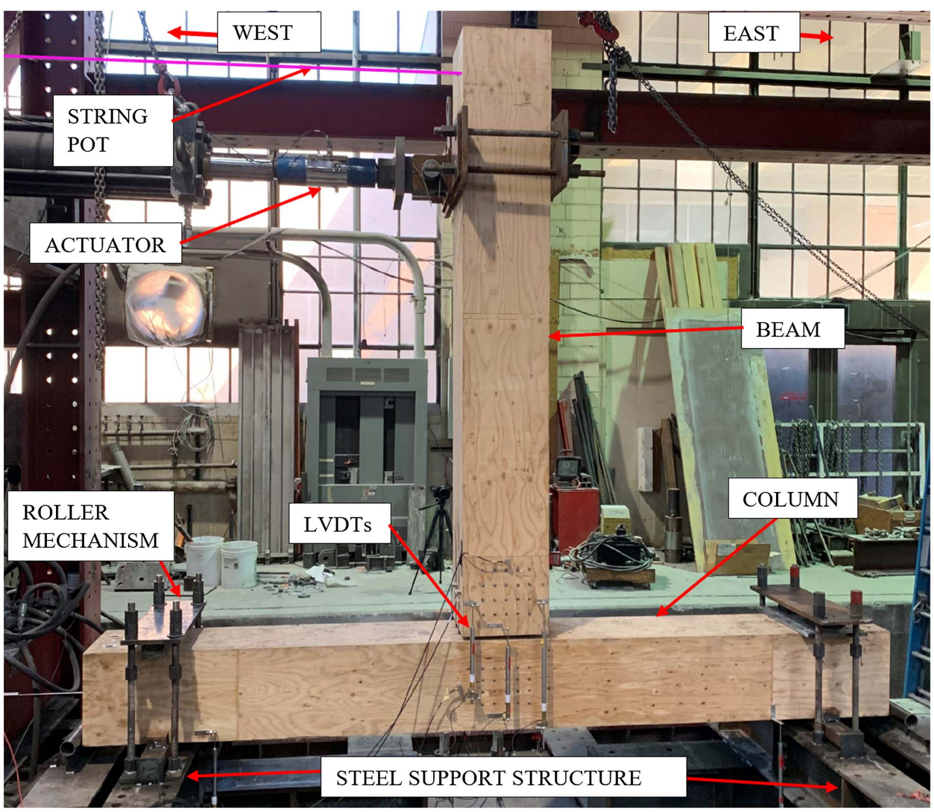


**Fig. 6.** Experimental testing configuration.

Lam et al. 2008), the rotation appears to be limited because the contact between the column and the beam caused timber crushing and splitting around the dowels, therefore leading the joint to fail. A 25 mm (1-in.) gap with a 381 mm (15-in.) deep beam theoretically allows for 0.13 radians (7.4 degrees) of rotation before contact is made. This exceeds the rotation capacity of typical shear-plate connections in a steel building under cyclic rotations, which could reach 0.09 radians (5.2 degrees) (Astaneh-Asl 2005). The gap allowed us to see how large a rotation a timber connection could achieve and informs the rotational ductility of the entire system.

## Testing Program

For testing convenience, the joint circled in Fig. 1 was rotated 1.57 radians (90 degrees) counterclockwise and the load was applied horizontally to the beam by a hydraulic actuator at the theoretical inflection point, as shown in Fig. 6. The actuator was clamped to the beam with steel plates on both sides, which were connected with four threaded rods. This attachment allowed the actuator to apply both monotonic and cyclic loading protocols. Large plates were selected to avoid localized timber crushing of the beam at the load application site.

The column was supported at each end by a rocker mechanism, shown in Fig. 7(b), to allow rotation, which is expected at points of inflection when a lateral load is applied to a frame. The base of the rocker mechanism is a steel plate with a 64 mm (2.5 in.) diameter half-cylinder. A half-moon shaped steel plate was placed on top to complete the rocker mechanism. Grease was applied to the half-cylinder and the inside of the half-moon steel piece to reduce friction and allow for the anticipated rotation. The assembly was placed on top of the steel support structure below the column, and upside down on top of the column, as shown in Fig. 7(a). Threaded rods extended from the top rocker mechanism down to the steel support structure to prevent uplift at the column ends. Finally, a 57 mm (2.25 in.) diameter steel tube stopper was placed at the east and west faces of the column to limit joint shifting during testing. The tube was chosen for its round shape to prevent the stopper from interfering with the rotation at each column end.

Two series of tests were completed: three monotonic tests and three cyclic tests. A displacement-controlled loading protocol applied the load at a rate of 3.2 mm/min (0.125 in./min) in the monotonic tests. At 25 mm (1-in.) increments, the test was paused to allow for closer observation of the joint. Each beam end was pushed to 245 mm (10 in.) of displacement, which was the maximum stroke allowed by the actuator. The cyclic tests used a loading protocol based on ASTM E2126 test method B (ASTM 2011), which defines loading procedures for timber cyclic tests, as shown in Fig. 8. The first four cycles were applied at a loading rate of 61 mm per minute (2.4 in. per minute). These cycles reached a peak displacement once in each direction before moving on to the next cycle. Positive displacement occurred when the actuator was pushing to the east, and negative displacement occurred when the actuator was pulling to the west, as shown in Fig. 6. The remaining cycles were applied at a loading rate of 122 mm per minute (4.8 in. per minute), and each peak displacement was repeated three times before increasing to the next peak displacement. The test was paused at the end of each step in peak displacement to survey the joint for any damage.

Each joint was instrumented using a string pot, strain gauges, and linear variable differential transformers (LVDT). The string pot was connected to the west face of the beam above the actuator and was based on the reaction frame above the actuator. There were

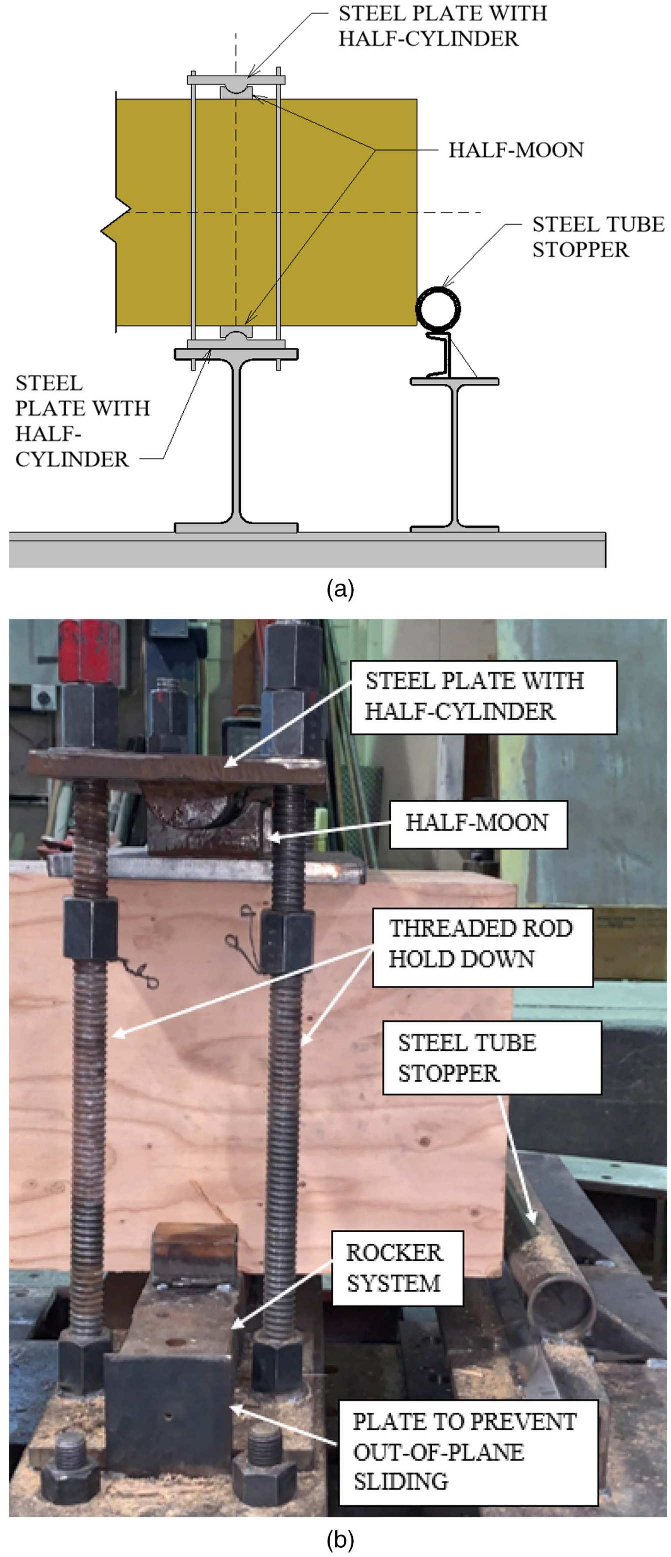


**Fig. 7.** Rocker mechanism at column ends: (a) schematic; and (b) experimental configuration.

three strain gauges attached to each plate in the gap between the beam and the column, on the east, west and center of the plate. LVDTs were placed on the south face of the joint to measure localized rotations. There was also an LVDT placed horizontally from the reaction frame to the west end of the column. Additionally, LVDTs were placed near each roller mechanism to measure the

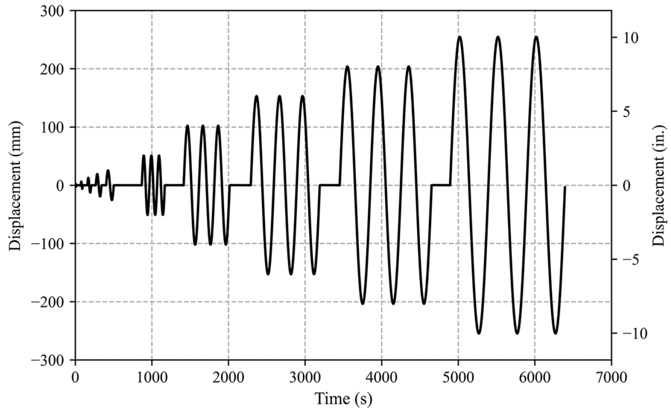


**Fig. 8.** Cyclic loading protocol.

vertical displacement, to confirm the column rotated as expected. Finally, an LVDT was placed on the bottom face of the column at the center connected to the support structure to measure the sag of the joint.

## Experimental Results

Three monotonic and three cyclic tests were completed using MPL beam-column joints with two slotted-in steel plates and a variety of steel dowel layouts in the beam. The bending moment developed in each joint was calculated using the load applied by the actuator. The rotation was calculated using the displacement measured by the string pot. Each joint achieved a rotation of at least 0.11 radians (6.3 degrees) at the maximum displacement with no visible timber splitting on the exterior of the connection.

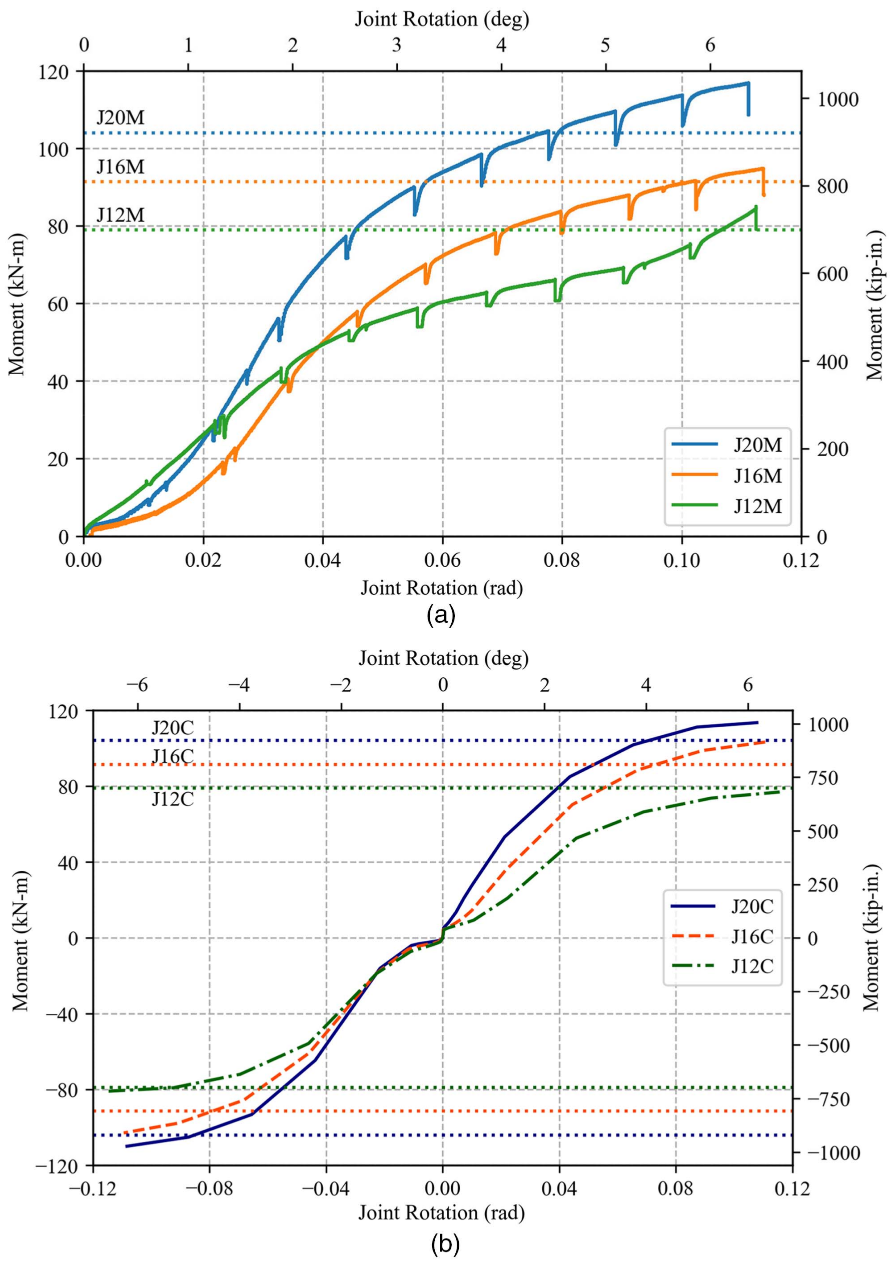


**Fig. 9.** Experimental results: (a) monotonic tests; and (b) cyclic tests.

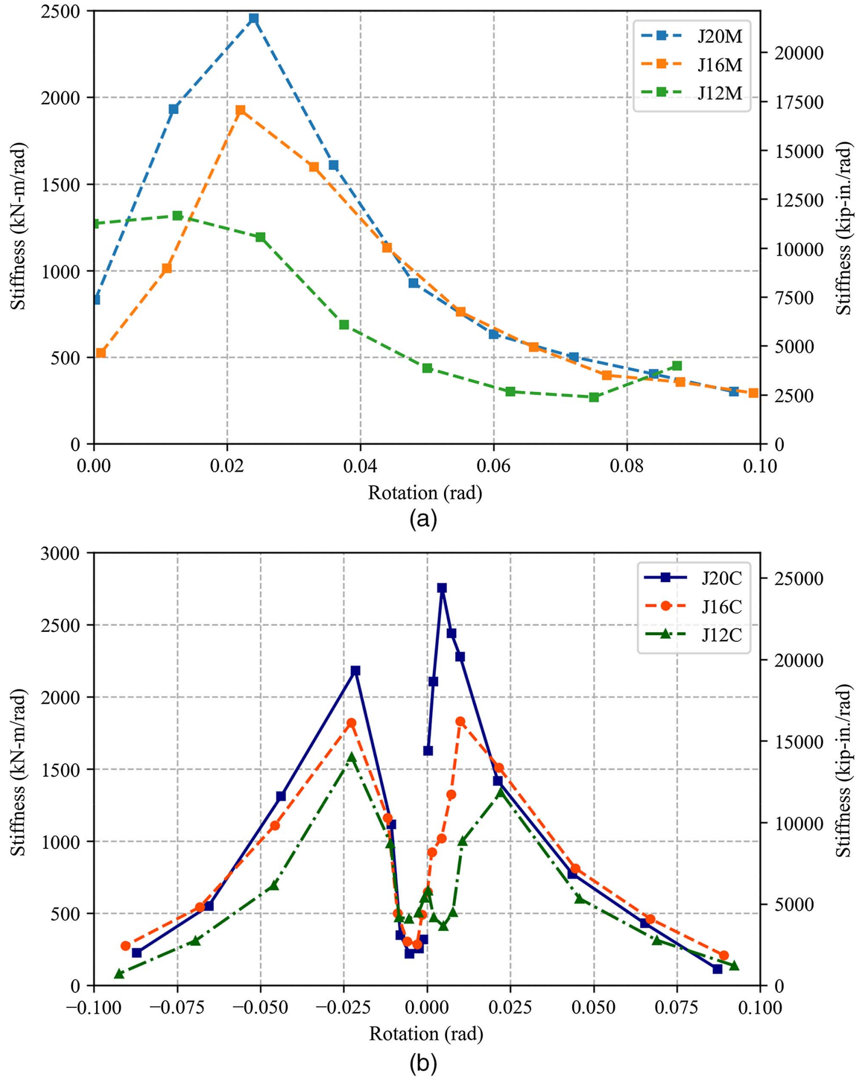


**Fig. 10.** Joint stiffness: (a) monotonic tests; and (b) cyclic tests.

### *Moment-Rotation Curves*

The moment-rotation curves from the monotonic tests are shown in Fig. 9(a). The dashed horizontal lines represent the theoretical bending moment capacity of each joint listed in Table 2. All three joints eventually achieved the theoretical moment, although joints with fewer dowels did not reach capacity until larger rotations. The large sharp dips in the curves occurred when the actuator restarted after pausing the test for observation. There are also some smaller dips that occurred during testing when the force overcame the friction and the entire joint shifted between the column end stoppers.

The cyclic envelopes of the cyclic tests are shown in Fig. 9(b). Similar to the monotonic tests, the maximum bending moment capacity of the joint was approximately proportional to the number of dowels in the beam. The cyclic tests generally developed higher

**Table 3.** Yield point and ductility for all joints using the Y&K method

| | Maximum point | | Yield point | | |
|---|---|---|---|---|---|
| Joint | $M_u$ kN-m (kip-in.) | Rotation rad (degrees)[a] | $M_y$ kN-m (kip-in.) | Rotation rad (degrees) | Ductility |
| 20M | 117 (1,034) | 0.11 (6.3) | 77 (679) | 0.043 (2.5) | 2.59 |
| 16M | 95 (839) | 0.11 (6.3) | 58 (509) | 0.045 (2.6) | 2.53 |
| 12M | 85 (753) | 0.11 (6.3) | 49 (435) | 0.036 (2.1) | 3.08 |
| 20C+ | 113 (1,004) | 0.11 (6.3) | 64 (570) | 0.026 (1.5) | 4.05 |
| 20C- | −110 (−972) | −0.11 (−6.3) | −68 (−605) | −0.047 (−2.7) | 2.32 |
| 16C+ | 103 (915) | 0.11 (6.3) | 63 (562) | 0.038 (2.2) | 2.93 |
| 16C- | −103 (−910) | −0.11 (−6.3) | −68 (−606) | −0.053 (−3.0) | 2.07 |
| 12C+ | 77 (681) | 0.12 (6.9) | 69 (612) | 0.067 (3.8) | 1.73 |
| 12C- | −81 (−716) | −0.12 (−6.9) | −74 (−656) | −0.065 (−3.7) | 1.77 |

[a]Maximum rotation reached during the test without failure of the joints.

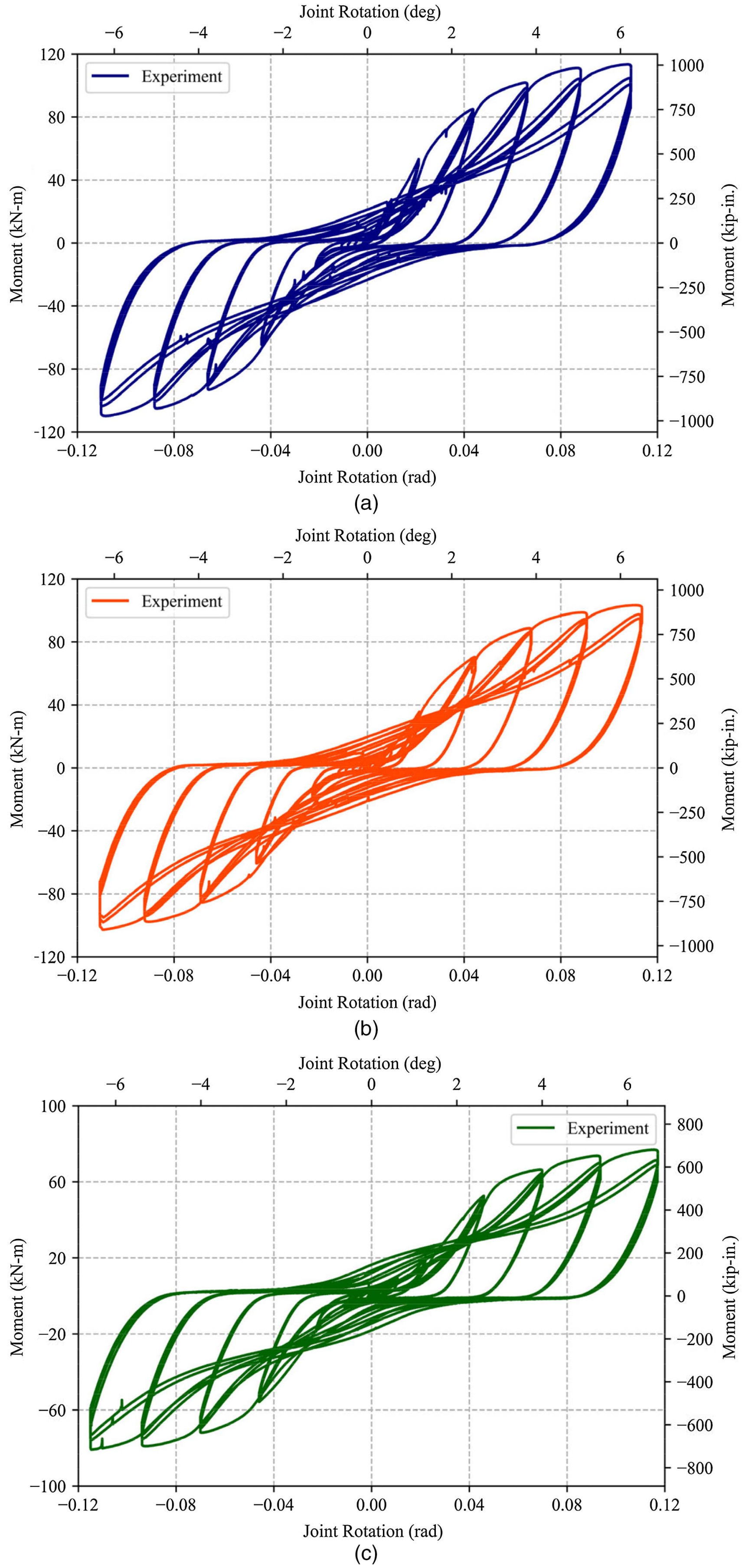


**Fig. 11.** Cyclic experimental results: (a) joint 20C; (b) joint 16C; and (c) joint 12C.

peak stiffnesses than did the monotonic tests. This is because of the additional force it takes to straighten and re-bend the dowels in the opposite direction when the load is reversed.

### Joint Slip

In general, there are three stages that can be identified in the moment-rotation curves. The first stage is an initial slip, which occurred at small rotations. This slip is common for timber connections with dowel connectors, and it occurs as a result of the construction tolerances and irregularities of the timber within the connection. The holes in the timber and steel plates are slightly oversized to accommodate the dowel, so some displacement occurs before the dowels make full contact; this contact engages the members and allows the connection to develop stiffness. Joint 12M did not experience this initial slip stage [Fig. 9(a)]; this may be because the small number of dowels in the beam forced them to immediately engage with the timber. This slip was not as pronounced for the positive direction of the joints tested with cyclic loads [Fig. 9(b)], hence the slip may be related more to the construction tolerance of the dowel holes and friction between the steel plates and the timber.

### Stiffness

The next stage of the moment-rotation curve is the elastic portion; in this part of the curve, the stiffness reaches its peak, as shown in Fig. 10. Similar to the maximum moment, the maximum stiffness decreases with fewer dowels in the beam. The final stage of the moment-rotation curve is the post-yield portion; at this stage, the stiffness of the connection decreases significantly, thus preventing the joint from developing larger moments with increased rotation. Contact between the beam and column members was observed during the third test, which caused an increase in stiffness during the post-yield stage beginning at 0.09 radians (5.2 degrees) [Fig. 10(a)].

### Ductility

The yield point for all joints was estimated using the Y and K method (Yasumura and Kwai 1998), as shown in Table 3. Shen et al. (2021) evaluated the yield point of timber connections and concluded that the Y and K method most accurately represents the yield point for timber connections. The rotational ductility of each connection was also determined by dividing the maximum rotation by the rotation at the yield point. This ductility is a lower bound estimate of the joint ductility because the actuator reached its maximum stroke before the joint experienced any loss in load.

### Hysteresis Curves

The hysteresis curves for the cyclic tests are shown in Fig. 11. The first few cycles at small displacements resulted in unbalanced hysteresis curves. The part of the curve related to the displacement in the east direction appeared to be much stiffer than the displacement in the west direction; this is likely due to the fact that the test began with pushing. To move in the east direction, the dowels had to engage with the timber, thus requiring more force to rotate due to the additional resistance caused by the timber. When the loading was reversed, only about half the force was required to reach the same rotation because there was a larger gap between the dowels and the timber to overcome before the dowels fully engaged with the timber in the other direction.

Eventually, the hysteresis curves achieved balanced moments in the east and west directions. This is when the dowels began to yield and the force in the joint depended more on how much force it took to bend the dowels rather than just the force required to engage the timber. It was also observed that the stiffness decreased during the second and third cycle of a step compared to the first cycle at that displacement. This is because the dowels had already crushed the timber in that direction during the first cycle at that displacement; because it took more displacement for the dowels to fully engage with the timber in the subsequent cycles, the stiffness decreased. Pinching of the hysteresis curve occurred for all three dowel layouts. The joints dissipated hysteretic energy nearly proportional to the number of dowels in the beam, as shown in Fig. 12.

### Joint Damage Observations

Fig. 13 shows each dowel layout at the maximum displacement imposed by the actuator. The strain on the steel plates measured by the strain gauges during the tests remained below 40% of the yield

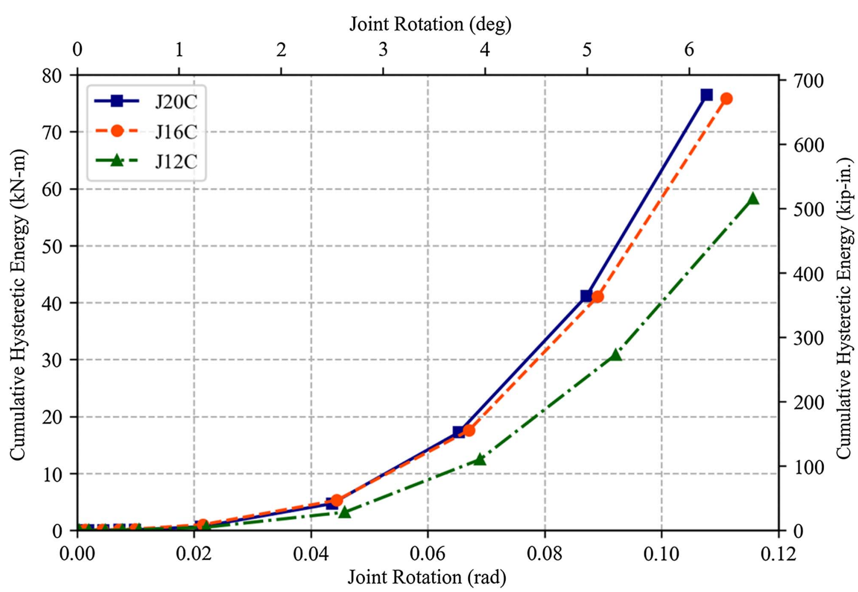


**Fig. 12.** Cumulative hysteretic energy.

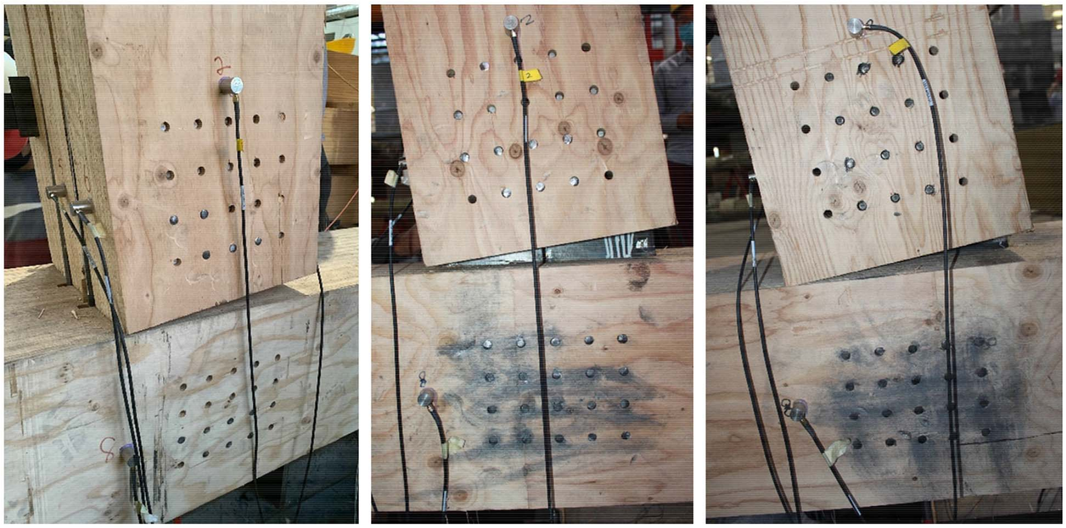

(a) (b) (c)

**Fig. 13.** Joints at maximum displacement: (a) joint 20M; (b) joint 16M; and (c) joint 12M.

strain. This occurred because the plate remained rigid while most of the plate deformation was localized around the dowel holes.

Observations of the joints during testing suggest that the center of rotation shifts depending on the number of dowels in the beam. During all of the monotonic tests, it seems much of the rotation occurs within the beam because the top west corners of the steel plates were exposed as the actuator applied more load as shown in Fig. 14(a). The test of joint 20M suggests that part of the rotation was also due to the rotation of the plate within the column, because as the rotation increased, the bottom east corner of the steel plates began to extend beyond the face of the column [Fig. 14(b)]. In comparison, Fig. 14(c) shows the plates in joint 16M experienced very little rotation within the column; the same was observed for joint 12M.

Joint 12M developed a small indentation in the column once the beam made contact with it at 0.09 radians (5.2 degrees). The increased stresses caused by the contact caused minor timber crushing at the corner of the beam, as shown in Fig. 15.

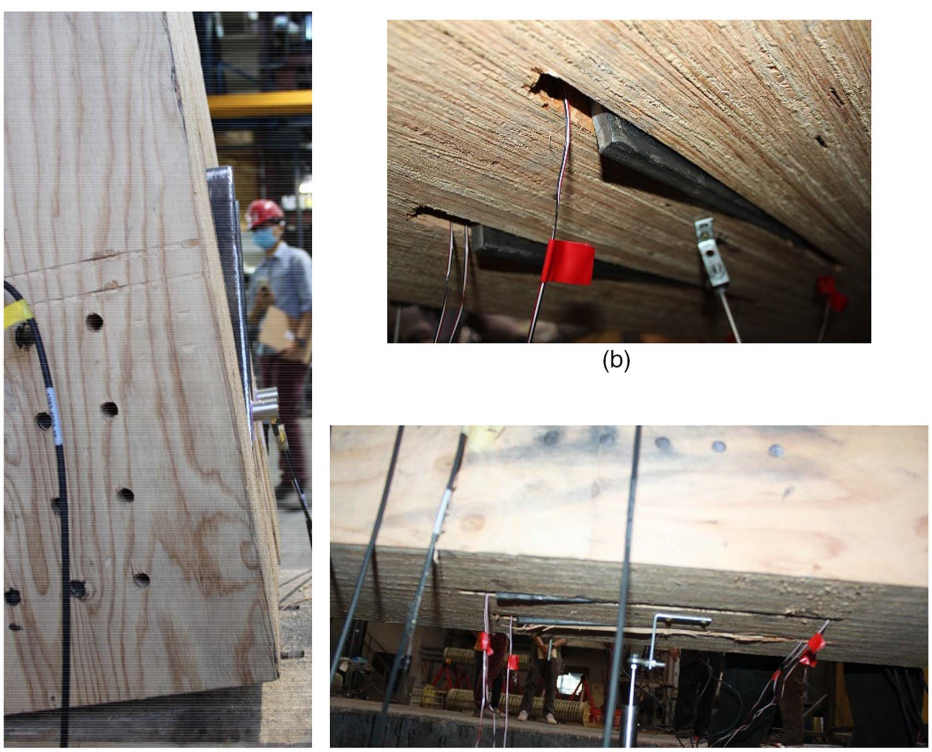

(a) (b) (c)

**Fig. 14.** Joint rotation observations: (a) plates extend beyond west face of beam; (b) plate extension beyond joint 20M column; and (c) plate extension beyond joint 16M column.

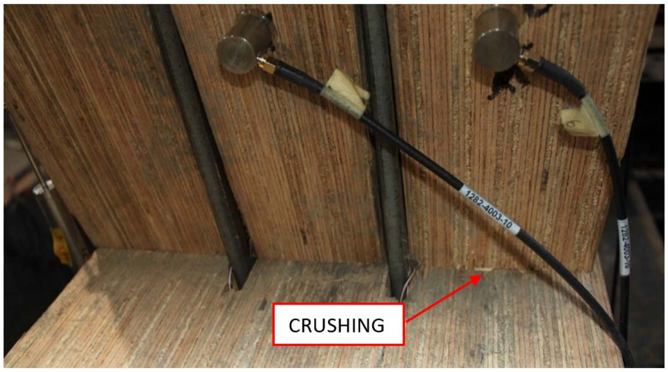


**Fig. 15.** Contact between beam and column for joint 12M.

After testing was completed, the joints were dissected and inspected for internal damage. The dowels in joints that were placed under monotonic loading were observed to have failed in mode IV, as expected based on the design of the connections. Fig. 16(a) shows bending of a dowel following testing compared to an identical straight dowel. Although minimal dowel yielding occurred, bending within the steel plates [shown with silver marks on the dowel in Fig. 16(a)] can be seen. This suggests the dowels experienced yield mode four behavior. The dowels were observed to be bent in the direction of rotation, as shown in Fig. 16(b). Moreover, the most extreme bending was observed in the dowels that were farthest away from the center of rotation, as shown in Fig. 16(c).

Similarly to the monotonic tests, the joints tested under cyclic loading were dissected when testing was complete. The joints tested under cyclic loads were loaded with twenty cycles and did not experience any fracture from low cycle fatigue. The dowels in these tests showed similar bending characteristics to the monotonic tests although bending was not as extreme, as shown in Fig. 17(a). This was because the beam returned to center to complete the last cycle of the test, so the dowels were slightly bent back straight. Although bending was not as pronounced in the dowel for the cyclic load tests, necking was observed in the dowel where it intersected the plate due to repeated cycles [Fig. 17(b)]. This implies that the dowels in the cyclic tests also yielded in mode IV as designed. In addition to necking, damage to the steel plates near the dowel holes was observed [Fig. 17(c)]. The hole was elongated where the dowel bent and made contact with the steel plate. The angle of the damage and hole elongation is consistent with the expected direction of the force vector in the dowel suggested by the model described by Bouchaïr et al. (2007).

## Numerical Model

An OpenSees (McKenna et al. 2010) numerical model for each dowel layout of the cyclic tests was developed and validated using the experimental results. The model was defined with five nodes, as shown in Fig. 18. Beam and column members were modeled with *ForceBeamColumn* elements; they were modeled as elastic sections, because the beam and column remained elastic outside of the connection. The column ends were pinned to replicate the end conditions during the experiments. The connection, including the steel plates, dowels and timber, was modeled using a *twoNodeLink* with zero length. The connection behavior was represented by the *pinching4 material*, which is often used to define the hysteretic behavior of a material. The moment-rotation relationship for the monotonic tests was defined using three points of significance along the experimental moment-rotation curve: the point when the initial slip was approximately completed, the yield point calculated previously, and the point at the maximum moment. The moment-rotation relationship for the cyclic tests was defined using the positive envelope from each joint placed under cyclic loading. The remaining parameters were then adjusted to most accurately capture the unloading and reloading stiffness observed during testing.

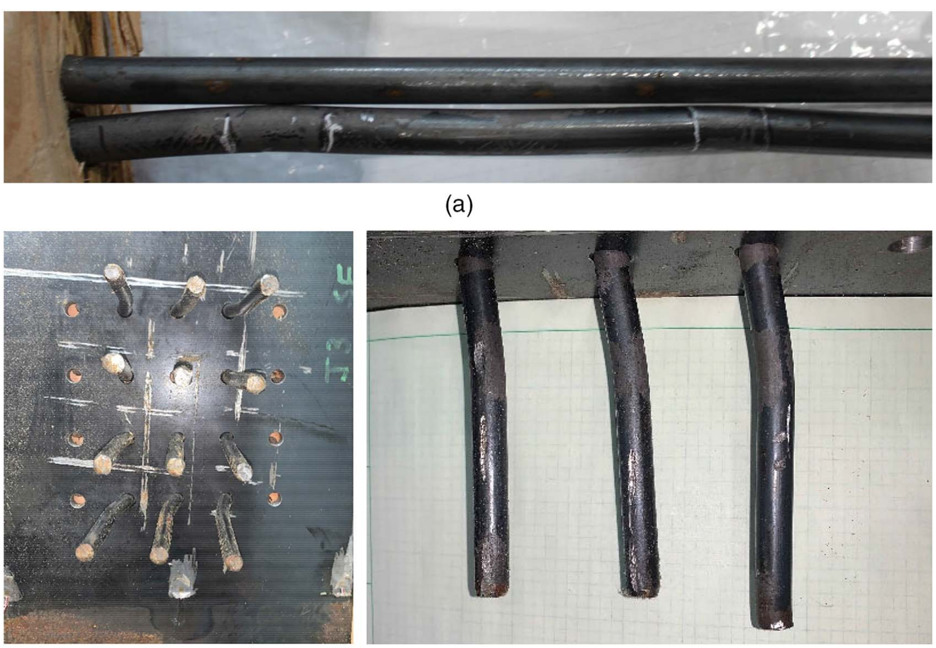

(a)

(b)

(c)

**Fig. 16.** Mode IV yielding of dowels: (a) dowel in beam joint 20M; (b) elevation of dowels joint 12M; and (c) plan view of top row of dowels joint 12M.





J. Struct. Eng., 2023, 149(6): 04023057


**Fig. 17.** Damage to joint 12C: (a) bending; (b) necking; and (c) hole elongation.



The load was applied to the end of the beam using a displacement-controlled loading command. To replicate the experimental results, the end of the beam was displaced to the same peak displacements and cycles according to the cyclic loading protocol, as described earlier in this paper.

The model results are plotted with experimental results (Fig. 19) to show the agreement with the experimental results. Generally, the model accurately depicts the shape of the experimental hysteresis curve created during testing. Differences between the model and the experiment may be due to the internal friction of the actuator, which prevented it from always reaching the exact specified displacement. By contrast, the model is idealized so it always reaches the specified displacement. The unloading stiffness of the model matches well with the unloading stiffness of the experimental results. The reloading stiffness is most accurate for the first cycle at each displacement; although adequate, it does not represent the subsequent cycles as well because the *pinching4 material* has limited input parameters. The reloading state in the model material is defined by a trilinear curve; however, the reloading state of the experimental curve includes an additional section when the reloading stiffness increases again as the cycle approaches the peak rotation.

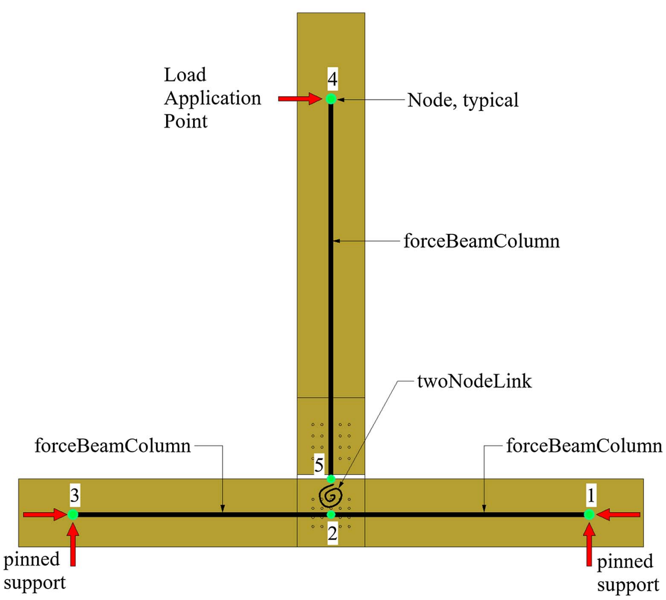


**Fig. 18.** OpenSees model layout.

The computational model has some limitations because one element is used to represent the entire connection, which is made of multiple dowels, steel plates, and timber sections. A much more rigorous finite element model is required to fully capture the response of the connection, including the yielding of the dowels and the localized timber crushing. However, such a detailed model may be challenging to validate due to the limited visibility and knowledge of the response of the dowels and timber during testing. The model described previously provides an acceptable representation of the connection moment-rotation relationship without requiring the large computational effort of a detailed finite element model. Further testing is required to accurately calibrate a model to represent the connection resistance to the axial and shear forces in the beam and columns. This computational model represents only the moment-rotation relationship of the connection because that was the focus of this testing program; however, it is very useful for the analysis of TBRB frames such as the one shown in Fig. 1. The computational model can be expanded in the future to address shear deformations.

## Discussion

Three monotonic and three cyclic beam-column joint tests were completed in the experimental program. All of the joints achieved a maximum rotation of 0.11 radians (6.3 degrees) and performed in a ductile manner. The tests showed that the bending moment resisted by each joint was approximately proportional to the number of the dowels in the beam. This is what was expected based on the design of the connections. Even though the number of dowels affected the amount of force the joint was able to resist, it did not impact the joint's ability to achieve high rotation without visible external damage to the timber. A key aspect of the design that allowed the joints to achieve satisfactory rotations was the 25 mm (1.0 in.) gap provided between the end of the beam and the face of the column; this gap, which depends on the section depth, allowed the beam to rotate without making contact with the column. Avoiding additional stress caused by the contact helped prevent timber splitting perpendicular to grain, which has been observed during previous tests completed by other researchers (Dong et al. 2021; Lam et al. 2008).

Unlike previously completed tests, these joints did not require additional joint reinforcement to prevent perpendicular-to-grain splitting when the joint was loaded; this is due to the cross-ply layup of the MPL used for the beams and columns in these tests. This property has the potential to significantly reduce the cost of



J. Struct. Eng., 2023, 149(6): 04023057

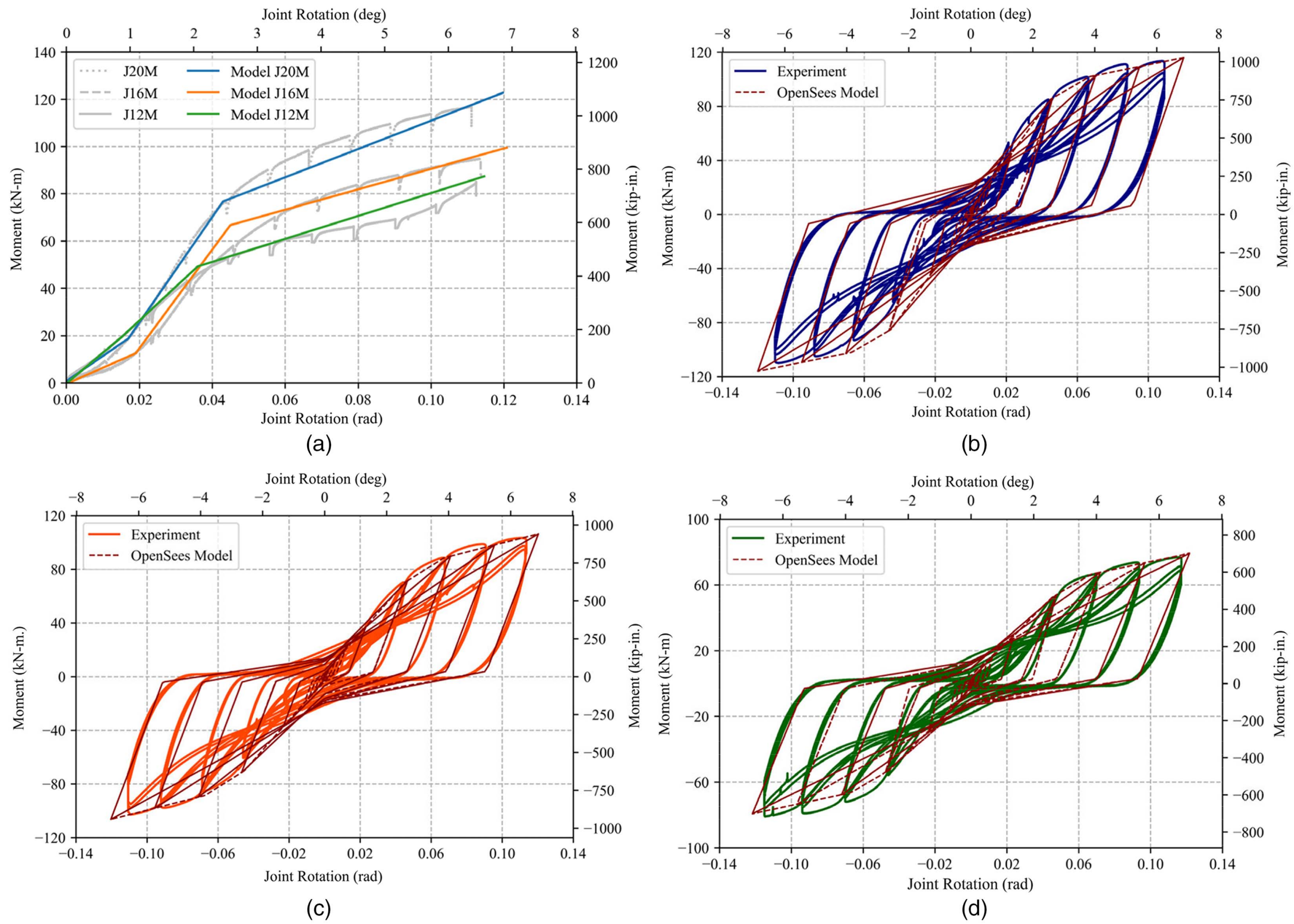


**Fig. 19.** OpenSees model comparisons to experiment: (a) joints 20M, 16M, 12M; (b) joint 20C; (c) joint 16C; and (d) joint 12C.

each connection by requiring fewer fasteners compared to similar connections with different classifications of timber.

## Conclusions

Based on the results of the experimental program and the simple computational model developed in this study, the following conclusions can be drawn:

- The design of the joint using established procedures and published research resulted in a ductile response of the joints.
- The 25 mm (1-in.) gap between the beam end and column face, which depends on the section depth, allowed the joint to achieve high rotations by preventing additional stresses caused by contact between the timber members.
- The cross-ply layup of MPL helps prevent perpendicular to grain splitting, thus eliminating the need for additional joint reinforcement.
- The joints were subjected to twenty cycles without fatigue fracture of any of the dowels. The dowels yielded but the steel plates only reached 40% of the yield strain.
- The joints achieved a maximum rotation of 0.11 radians (6.3 degrees), which is satisfactory, without a reduction in strength.
- The maximum bending moment capacity of the joints tested under monotonic or cyclic loads was approximately proportional to the number of dowels in the beam.
- The maximum stiffness of the joints tested under monotonic or cyclic loads decreases with fewer dowels in the beam.
- The joints tested under cyclic loads dissipated hysteretic energy nearly proportionally to the number of dowels in the beam.
- The rotational ductility of each connection, determined using the Y&K method, ranged from 1.8 to 4.0.
- A phenomenological model was developed using simple elements, which predicted the monotonic and cyclic response of the joints in a satisfactory manner and could be used to model such joints in TBRB frames.

## Data Availability Statement

Some or all data, models or code that supports the findings of this study are available from the corresponding author upon reasonable request.

## Acknowledgments

The authors would like to acknowledge the financial support provided by Wood Innovations under USDA Grant 20-DG-11046000-615. The authors also acknowledge the donation of materials by Freres Lumber Co., and the in-kind assistance provided by the Timberlab. The authors acknowledge the assistance of M. Bryant, D. Tran,

I. Dangol, D. Briggs, S. Neupane, and S. Shrestha of the University of Utah for their assistance in carrying out the experiments.

## References

AISC. 2016. *Seismic provisions for structural steel buildings*. ANSI/AISC 341-16. Chicago: AISC.

APA (Engineered Wood Association). 2021. *Freres mass ply panels (MPP), and mass ply lam (MPL) beams and columns*. Rep. No. PR-L325. Tacoma, WA: APA—The Engineered Wood Association.

ASCE. 2016. *Minimum design loads and associated criteria for buildings and other structures*. ASCE 7-16. Reston, VA: ASCE.

Astaneh-Asl, A. 2005. *Design of shear tab connections for gravity and seismic loads*. Moraga, CA: Structural Steel Education Council.

ASTM. 2011. *Standard test methods for cyclic (reversed) load test for shear resistance of vertical elements of the lateral force resisting system for buildings*. ASTM E2126. West Conshohocken, PA: ASTM.

ASTM. 2019. *Standard specification for evaluation of structural composite lumber products*. ASTM D5456. West Conshohocken, PA: ASTM.

AWC (American Wood Council). 2018a. *General dowel equations for calculating lateral connection values with Appendix A*. Technical Rep. No. 12. Leesburg, VA: AWC.

AWC (American Wood Council). 2018b. *National design specification for wood construction*. Leesburg, VA: AWC.

Black, C. J., N. Makris, and I. D. Aiken. 2004. "Component testing, seismic evaluation and characterization of buckling-restrained braces." *J. Struct. Eng.* 130 (6): 880–894. https://doi.org/10.1061/(ASCE)0733-9445(2004)130:6(880).

Blaß, H. J., and P. Schädle. 2011. "Ductility aspects of reinforced and non-reinforced timber joints." *Eng. Struct.* 33 (11): 3018–3026. https://doi.org/10.1016/j.engstruct.2011.02.001.

Blomgren H.-E., J.-P. Koppitz, A. D. Valdes, and E. Ko. 2016. "The heavy timber buckling-restrained brace frame as a solution for commercial buildings in regions of high seismicity." In *Proc., World Conf. on Timber Engineering*. Vienna, Austria: Institute for Mechanics of Materials and Structures.

Bouchaïr, A., P. Racher, and J. F. Bocquet. 2007. "Analysis of dowelled timber to timber moment-resisting joints." *Mater. Struct.* 40 (10): 1127–1141. https://doi.org/10.1617/s11527-006-9210-0.

Cao, J., H. Xiong, and Y. Cui. 2022. "Seismic performance analysis of timber frames based on a calibrated simplified model." *J. Build. Eng.* 46 (Apr): 103701. https://doi.org/10.1016/j.jobe.2021.103701.

Daneshvar, H., J. Niederwestberg, J.-P. Letarte, and Y. H. Chui. 2022. "Yield mechanisms of base shear connections for cross-laminated timber shear walls." *Constr. Build. Mater.* 335 (Jun): 127498. https://doi.org/10.1016/j.conbuildmat.2022.127498.

Dong, W., M. Li, M. He, and Z. Li. 2021. "Experimental testing and analytical modeling of glulam moment connections with self-drilling dowels." *J. Struct. Eng.* 147 (5): 04021047. https://doi.org/10.1061/(ASCE)ST.1943-541X.0002977.

Dong, W., M. Li, C.-L. Lee, G. MacRae, and A. Abu. 2020. "Experimental testing of full-scale glulam frames with buckling restrained braces." *Eng. Struct.* 222 (Nov): 111081. https://doi.org/10.1016/j.engstruct.2020.111081.

Dorn, M., K. de Borst, and J. Eberhardsteiner. 2013. "Experiments on dowel-type timber connections." *Eng. Struct.* 47 (Feb): 67–80. https://doi.org/10.1016/j.engstruct.2012.09.010.

Fahnestock, L. A., R. Sause, and J. M. Ricles. 2007. "Seismic response and performance of buckling-restrained braced frames." *J. Struct. Eng.* 133 (9): 1195–1204. https://doi.org/10.1061/(ASCE)0733-9445(2007)133:9(1195).

Fan, X., S. Zhang, and W. Qu. 2011. "Load-carrying behaviour of dowel-type timber connections with multiple slotted-in steel plates." *Appl. Mech. Mater.* 94–96 (8): 43–47. https://doi.org/10.4028/www.scientific.net/AMM.94-96.43.

FPL (Forest Products Laboratory). 2010. *Wood handbook—Wood as an engineering material*. General Technical Rep. No. FPL-GTR-190. Madison, WI: FPL.

Fragiacomo, M., and M. Batchelar. 2012. "Timber frame moment joints with glued-in steel rods. I: Design." *J. Struct. Eng.* 138 (6): 789–801. https://doi.org/10.1061/(ASCE)ST.1943-541X.0000419.

Geiser, M., M. Bergmann, and M. Follesa. 2021. "Influence of steel properties on the ductility of doweled timber connections." *Constr. Build. Mater.* 226 (Jan): 121152. https://doi.org/10.1016/j.conbuildmat.2020.121152.

Hashemi, A., H. Bagheri, S. M. M. Yousef-Beik, F. M. Darani, A. Valadbeigi, P. Zarnani, and P. Quenneville. 2020. "Enhanced seismic performance of timber structures using resilient connections: Full-scale testing and design procedure." *J. Struct. Eng.* 146 (9): 04020180. https://doi.org/10.1061/(ASCE)ST.1943-541X.0002749.

Hashemi, A., R. Masoudnia, and P. Quenneville. 2016. "Seismic performance of hybrid self-centering steel-timber rocking core walls with slip friction connections." *J. Constr. Steel Res.* 126 (Nov): 201–213. https://doi.org/10.1016/j.jcsr.2016.07.022.

Hashemi, A., P. Zarnani, R. Masoudnia, and P. Quennneville. 2018. "Experimental testing of rocking cross-laminated timber walls with resilient slip friction joints." *J. Struct. Eng.* 144 (1): 04017180. https://doi.org/10.1061/(ASCE)ST.1943-541X.0001931.

Kiggins, S., and C.-M. Uang. 2006. "Reducing residual drift of buckling-restrained braced frames as a dual system." *Eng. Struct.* 28 (11): 1525–1532. https://doi.org/10.1016/j.engstruct.2005.10.023.

Lam, F., M. Schulte-Wrede, C. C. Yao, and J. J. Gu. 2008. "Moment resistance of bolted timber connections with perpendicular to grain reinforcements." In *Proc., World Conf. on Timber Engineering, Institute for Mechanics of Materials and Structures*. Madison, WI: Engineered Wood Products Association.

McKenna, F., M. H. Scott, and G. L. Fenves. 2010. "Nonlinear finite-element analysis software architecture using object composition." *J. Comput. Civ. Eng.* 24 (1): 95–107. https://doi.org/10.1061/(ASCE)CP.1943-5487.0000002.

Murphy, C., C. P. Pantelides, H.-E. Blomgren, and D. Rammer. 2021. "Development of timber buckling restrained brace for mass timber-braced frames." *J. Struct. Eng.* 147 (5): 04021050. https://doi.org/10.1061/(ASCE)ST.1943-541X.0002996.

Ogrizovic, J., F. Wanninger, and A. Frangi. 2017. "Experimental and analytical analysis of moment-resisting connections with glued-in rods." *Eng. Struct.* 145 (Aug): 322–332. https://doi.org/10.1016/j.engstruct.2017.05.029.

Otero-Chans, D., J. Estévez-Cimadevila, F. Suárez-Riestra, and E. Martín-Gutiérrez. 2018. "Experimental analysis of glued-in steel plates used as shear connectors in Timber-Concrete-Composites." *Eng. Struct.* 170 (Sep): 1–10. https://doi.org/10.1016/j.engstruct.2018.05.062.

Petrycki, A., and O. Salem. 2020. "Structural integrity of bolted glulam frame connections reinforced with self-tapping screws in a column removal scenario." *J. Struct. Eng.* 146 (10): 04020213. https://doi.org/10.1061/(ASCE)ST.1943-541X.0002792.

Popovski, M., H. G. L. Prion, and E. Karacabeyli. 2002. "Seismic performance of connections in heavy timber construction." *Can. J. Civ. Eng.* 29 (3): 389–399. https://doi.org/10.1139/l02-020.

Rebouças, A. S., Z. Mehdipour, J. M. Branco, and P. B. Lourenço. 2022. "Ductile moment-resisting timber connections: A review." *Buildings* 12 (2): 240. https://doi.org/10.3390/buildings12020240.

Sabelli, R., S. A. Mahin, and C. Chang. 2003. "Seismic demands on steel braced-frame buildings with buckling-restrained braces." *Eng. Struct.* 25 (5): 655–666. https://doi.org/10.1016/S0141-0296(02)00175-X.

Shen, Y., J. Schneider, S. Tesfamariam, S. F. Stiemer, and Z. Chen. 2021. "Cyclic behavior of bracket connections for cross-laminated timber (CLT): Assessment and comparison of experimental and numerical models studies." *J. Build. Eng.* 39 (Jul): 102197. https://doi.org/10.1016/j.jobe.2021.102197.

Steiger, R., E. Serrano, M. Stepinac, V. Rajcic, C. O'Neill, D. McPolin, and R. Widmann. 2015. "Strengthening of timber structures with glued-in rods." *Constr. Build. Mater.* 97 (Oct): 90–105. https://doi.org/10.1016/j.conbuildmat.2015.03.097.

Wu, A.-C., P.-C. Lin, and K.-C. Tsai. 2014. "High-mode buckling responses of buckling-restrained brace core plates." *Earthquake Eng. Struct. Dyn.* 43 (3): 375–393. https://doi.org/10.1002/eqe.2349.

Xu, W., and C. P. Pantelides. 2017. "Strong-axis and weak-axis buckling and local bulging of buckling-restrained braces with prismatic core plates." *Eng. Struct.* 153 (Dec): 279–289. https://doi.org/10.1016/j.engstruct.2017.10.017.

Yasumura, M., and N. Kwai. 1998. "Estimating seismic performance of wood-frame structures." In *Proc., 5th World Conf. on Timber Engineering*, 564–571. Lausanne, Switzerland: Presses Polytechniques et Universitaires Romandes.